Research Article
Vol. 8, No. 6 | 1 Jun 2017 | BIOMEDICAL OPTICS EXPRESS 3110
Biomedical Optics EXPRESS

Looking inside the heart: a see-through view of the vascular tree

IMKE NEHRHOFF,[1] JORGE RIPOLL,[1,2] RAFAEL SAMANIEGO,[3] MANUEL DESCO,[1,2,4,5,*] AND MARIA VICTORIA GÓMEZ-GAVIRO[1,4]

[1] *Instituto de Investigación Sanitaria Gregorio Marañón, (IiSGM), Madrid, Spain,*
[2] *Departamento de Bioingenieria e Ingeniería Aeroespacial, Universidad Carlos III de Madrid, Spain*
[3] *Unidad de Microscopía Confocal, Instituto de Investigación Sanitaria Gregorio Marañón, Madrid, Spain*
[4] *Centro de Investigación Biomédica en Red de Salud Mental (CIBERSAM), Madrid, Spain*
[5] *Centro Nacional de Investigaciones Cardiovasculares (CNIC), Spain*
**mdesco@hggm.es*

Abstract: The ability to acquire 3D images of the heart and its vasculature at cellular resolution facilitates a more detailed study of many heart diseases. Here, we describe a novel technique to image in 3D the heart vasculature by combining the CUBIC clearing protocol combined with *in vivo* administration of fluorescent-labeled lectin. The use of these techniques in combination with *S*elective *P*lane *I*llumination *M*icroscopy (SPIM) made it possible to obtain high resolution 3D images of the cardiac vascular tree. This methodological approach may enhance the visualization of 3D images of the cardiac vasculature remodeling associated with coronary disease.

OCIS codes: (180.0180) Microscopy; (170.6930) Tissue; (170.6900) Three-dimensional microscopy; (170.3880) Medical and biological imaging.

References and links

1. J. B. Strait and E. G. Lakatta, "Aging-associated cardiovascular changes and their relationship to heart failure," Heart Fail. Clin. **8**(1), 143–164 (2012).
2. M. Rodriguez-Porcel, X. Y. Zhu, A. R. Chade, B. Amores-Arriaga, N. M. Caplice, E. L. Ritman, A. Lerman, and L. O. Lerman, "Functional and structural remodeling of the myocardial microvasculature in early experimental hypertension," Am. J. Physiol. Heart Circ. Physiol. **290**(3), 978–984 (2005).
3. A. J. Moy, P. C. Lo, and B. Choi, "High-resolution visualization of mouse cardiac microvasculature using optical histology," Biomed. Opt. Express **5**(1), 69–77 (2014).
4. R. Dickie, R. M. Bachoo, M. A. Rupnick, S. M. Dallabrida, G. M. Deloid, J. Lai, R. A. Depinho, and R. A. Rogers, "Three-dimensional visualization of microvessel architecture of whole-mount tissue by confocal microscopy," Microvasc. Res. **72**(1-2), 20–26 (2006).
5. P. J. Verveer, J. Swoger, F. Pampaloni, K. Greger, M. Marcello, and E. H. K. Stelzer, "High-resolution three-dimensional imaging of large specimens with light sheet-based microscopy," Nat. Methods **4**(4), 311–313 (2007).
6. S. Ivins, C. Roberts, B. Vernay, and P. J. Scambler, "Analysis of coronary vessels in cleared embryonic hearts," J. Vis. Exp., **118**, 54800 (2016).
7. I. Nehrhoff, D. Bocancea, J. Vaquero, J. J. Vaquero, J. Ripoll, M. Desco, and M. V. Gómez-Gaviro, "3D imaging in CUBIC-cleared mouse heart tissue: going deeper," Biomed. Opt. Express **7**(9), 3716–3720 (2016).
8. M. Sivaguru, G. Fried, B. S. Sivaguru, V. A. Sivaguru, X. Lu, K. H. Choi, M. T. Saif, B. Lin, and S. Sadayappan, "Cardiac muscle organization revealed in 3-D by imaging whole-mount mouse hearts using two-photon fluorescence and confocal microscopy," Biotechniques **59**(5), 295–308 (2015).
9. D. S. Richardson and J. W. Lichtman, "Clarifying tissue clearing," Cell **162**(2), 246–257 (2015).
10. E. A. Susaki, K. Tainaka, D. Perrin, H. Yukinaga, A. Kuno, and H. R. Ueda, "Advanced CUBIC protocols for whole-brain and whole-body clearing and imaging," Nat. Protoc. **10**(11), 1709–1727 (2015).
11. N. Jährling, K. Becker, and H. U. Dodt, "3D-reconstruction of blood vessels by ultramicroscopy," Organogenesis **5**(4), 227–230 (2009).
12. D. Dong, A. Arranz, S. Zhu, Y. Yang, L. Shi, J. Wang, C. Shen, J. Tian, and J. Ripoll, "Vertically scanned laser sheet microscopy," J. Biomed. Opt. **19**(10), 106001 (2014).
13. J. Schindelin, I. Arganda-Carreras, E. Frise, V. Kaynig, M. Longair, T. Pietzsch, S. Preibisch, C. Rueden, S. Saalfeld, B. Schmid, J.-Y. Tinevez, D. J. White, V. Hartenstein, K. Eliceiri, P. Tomancak, and A. Cardona, "Fiji: an open-source platform for biological-image analysis," Nat. Methods **9**(7), 676–682 (2012).

#291844 https://doi.org/10.1364/BOE.8.003110
Journal © 2017 Received 10 Apr 2017; revised 20 May 2017; accepted 21 May 2017; published 30 May 2017

14. A. Fedorov, R. Beichel, J. Kalpathy-Cramer, J. Finet, J.-C. Fillion-Robin, S. Pujol, C. Bauer, D. Jennings, F. Fennessy, M. Sonka, J. Buatti, S. Aylward, J. V. Miller, S. Pieper, and R. Kikinis, "3D Slicer as an image computing platform for the Quantitative Imaging Network," Magn. Reson. Imaging **30**(9), 1323–1341 (2012).
15. N. J. Tustison, B. B. Avants, P. A. Cook, Y. Zheng, A. Egan, P. A. Yushkevich, and J. C. Gee, "N4ITK: improved N3 bias correction," IEEE Trans. Med. Imaging **29**(6), 1310–1320 (2010).
16. M. K. Schwarz, A. Scherbarth, R. Sprengel, J. Engelhardt, P. Theer, and G. Giese, "Fluorescent-protein stabilization and high-resolution imaging of cleared, intact mouse brains," PLoS One **10**(5), e0124650 (2015).
17. H. Kolesová, M. Čapek, B. Radochová, J. Janáček, and D. Sedmera, "Comparison of different tissue clearing methods and 3D imaging techniques for visualization of GFP-expressing mouse embryos and embryonic hearts," Histochem. Cell Biol. **146**(2), 141–152 (2016).
18. M. V. Gómez-Gaviro, E. Balaban, D. Bocancea, M. T. Lorrio, M. Pompeiano, M. Desco, J. Ripoll, and J. J. Vaquero, "Optimized CUBIC protocol for 3D imaging of chicken embryos at single-cell resolution," Development dev.145805 (2017).
19. K. Tainaka, A. Kuno, S. I. Kubota, T. Murakami, and H. R. Ueda, "Chemical principles in tissue clearing and staining protocols for whole-body cell profiling," Annu. Rev. Cell Dev. Biol. **32**(1), 713–741 (2016).
20. E. A. Susaki, K. Tainaka, D. Perrin, F. Kishino, T. Tawara, T. M. Watanabe, C. Yokoyama, H. Onoe, M. Eguchi, S. Yamaguchi, T. Abe, H. Kiyonari, Y. Shimizu, A. Miyawaki, H. Yokota, and H. R. Ueda, "Whole-brain imaging with single-cell resolution using chemical cocktails and computational analysis," Cell **157**(3), 726–739 (2014).
21. A. Fedorov, R. Beichel, J. Kalpathy-Cramer, J. Finet, J. C. Fillion-Robin, S. Pujol, C. Bauer, D. Jennings, F. Fennessy, M. Sonka, J. Buatti, S. Aylward, J. V. Miller, S. Pieper, and R. Kikinis, "3D Slicer as an image computing platform for the Quantitative Imaging Network," Magn. Reson. Imaging **30**(9), 1323–1341 (2012).
22. A. Feuchtinger, A. Walch, and M. Dobosz, "Deep tissue imaging: a review from a preclinical cancer research perspective," Histochem. Cell Biol. **146**(6), 781–806 (2016).

1. Introduction

Coronary artery disease is accompanied by significant structural changes in the vascular network, including the thickening of large arteries, abnormal lipid deposits on the blood vessel wall and lumen narrowing [1].

These pathological changes may lead to a myocardial infarction and eventually to heart failure. Other pathologies such as hypertension are also associated with myocardial microvascular architecture changes [2]. Nowadays, there is a growing trend to study three-dimensional structure of intact tissues from actual 3D volumes, rather than analyzing thin tissue sections [3]. However, the acquisition of 3D images at cellular resolution to study the heart and its remodeling after disease still remains challenging. Confocal microscopy is a well-established technique to image and study tissues at cellular and subcellular resolution, and has been used to obtain microvascular imaging of different murine tissues [4]. However, confocal microscopy is well suited to generate 3D images of limited-thickness samples but not 3D images of whole organs. Overcoming the limited 3D abilities of confocal microscopy, Selective Plane Illumination Microscopy (SPIM) has been utilized to acquire three-dimensional information of large intact rodent organs [5]. Using optical tissue clearing and confocal microscopy Ivins et al. visualized coronary vessels in mouse embryonic hearts, after clearing the embryos with BABB and labelling endothelial cells with anti-CD31 [6]. However, protocols to obtain this kind of information in the adult heart are still missing.

A major obstacle for 3D-imaging of the adult heart is the opacity of the myocardial tissue. Since SPIM images are obtained through optical sectioning, it is of great importance to render the samples transparent prior to imaging, since opacity of the samples considerably limits the optical penetration depth (and therefore the spatial resolution) [7], due to changes in the refractive indices within the tissue and the resulting light scattering effects [8, 9].

In this work, we combined intra venous (i.v.) and intracardiac perfusion of fluorescently-tagged-lectins to label the mouse heart vasculature and rendered the tissue transparent using the *c*lear, *u*nobstructed *b*rain *i*maging *c*ocktails and *c*omputational analysis (CUBIC) clearing protocol [10]. The protocol presented here provides a pipeline to overcome the technical limitations of confocal microscopy by enabling the acquisition of high quality 3D images of the mouse heart at cellular resolution using SPIM. This preserves the 3D structure and cytoarchitecture of the heart.

2. Material and methods

We adapted the CUBIC clearing protocol for mouse heart and assessed the transparency, weight and sample volume at various time points during the clearing procedure. We carried out 3D image acquisition with SPIM, correcting the inhomogeneous illumination artifact typical of SPIM images with in-house developed software. Finally, we compared the image quality obtained with fluorophores that emit light at different wavelengths. All these steps are detailed in the next sub-sections.

2.1. Tissue clearing and immunohistochemistry

To obtain the heart samples, mice were transcardiacally perfused with 20 ml of ice cold phosphate buffered solution (PBS) followed by 50 ml of 4% paraformaldehyde (PFA) for at least 12 h [11]. The heart was extracted and post-fixed in 4% PFA overnight (o.n.). After perfusion, hearts were dissected, cut transversally or coronally with a surgical blade into two halves and post-fixed in 4% PFA o.n. Mouse heart halves were cleared by immersion in CUBIC-clearing reagent-1 (R1) for 5 days in a shaker at 80 rpm at 37°C. R1 consists of Urea, 2-hydroxypropyl, Triton X-100 and distilled water [10]. At day 4, R1 was replaced with fresh R1 containing DAPI (1:2500) and incubated for 2 more days. Afterwards, the heart halves were washed three times for 2 h with PBS at room temperature and were subsequently incubated with 0.02 mg/ml of anti-CD31 (ab28364, Abcam) in a shaker at 80 rpm at 37 °C for seven days. The antibody solution was renewed at day 3. After day 7 of antibody incubation, the tissue was washed three times, for 2 h each, with PBS-T (Triton 0,1% in PBS) at room temperature and incubated with 3.3 µg/ml of secondary antibody and 0.25 µg/ml of DAPI for seven days. The samples were then washed with PBS-T three times, for 2 h each, at room temperature and immersed in CUBIC-clearing reagent-2 (R2) for two days at 80 rpm and 37°C. R2 consists of Sucrose, Urea, Nitrilotriethanol and distilled water. The whole protocol is sketched in Fig. 1(A).

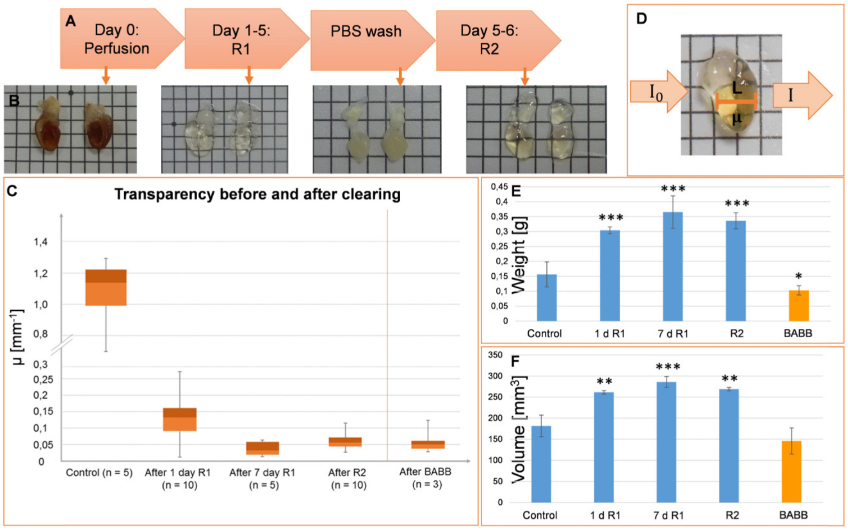

Fig. 1. CUBIC- and BABB-clearing in cardiac mouse tissue. A, Adapted CUBIC-clearing protocol for lectin-perfusion and clearing in mouse hearts. B, Stepwise enhancement of the sample transparency following the CUBIC-clearing protocol. C, Box-plot of the transparency measurement at different time points of the clearing protocol and at the end of BABB-clearing. D, Transparency measurement with Beer-Lambert law. I_0, initial light intensity; I, light intensity after traversing the uncleared/cleared tissue; L, tissue thickness; µ, absorption coefficient. E, F, Weight (E) and volume (F) measurements of the mouse hearts before, during and after the CUBIC- and BABB-clearing protocol. d, days in R1. n = 3. *$p<0.05$, **$p<0.005$, ***<0.0005, unpaired t-test vs control samples.

2.2. FITC-lectin labeling of heart vasculature

Adult male mice (n = 3) were anesthetized by intraperitoneal administration of Ketamine/Xylazine (80 mg/kg and 2 mg/kg, respectively). FITC-lectin was purchased from Sigma-Aldrich (L0401) and 649–lectin was purchased from Vector Laboratories (DL-1178). 0.3 ml of 0.52 µmol/L lectin stock were injected i.v. into the tail vein of the mice and left 5 min for circulation. The chest cavity of the animal was opened and 5 ml of 10 U/ml heparin in PBS were perfused transcardially, followed by 10 ml of 1% PFA. Next, another 10 ml of fluorescently-labeled lectin (10 µg-lectin/ml in PBS) were perfused for 3 minutes followed by a final perfusion of 30 ml 4% PFA. The hearts were dissected, post-fixed and treated as described in section 2.1.

2.3. Heart transparency and H&E staining

Transparency of the cleared hearts was measured using a set-up with a bright field microscope (Nikon Eclipse E800, Tokyo, Japan). The sample was illuminated with a light source from below and the light transmitted through the sample was captured through a Nikon Plan UW 2x objective (NA: 0.06, WD: 7.5mm) and recorded by a camera (Nikon Digital Camera DXM1200F, Tokyo, Japan). Two images were taken: one without the sample (representing I_0 in Eq. (1)) and another one with the sample in position (representing I in Eq. (1)). The transparency was calculated by solving the attenuation coefficient µ (that combines the effects of scattering and absorption) using the Beer-Lambert law:

$$I = I_0 e^{-\mu L} \tag{1}$$

Where L is the sample thickness crossed by the light along its path to the camera (Fig. 1D). Images were taken from three different regions of the sample, and the mean value and standard derivation of µ were computed.

For Hematoxilin&Eosin staining, after R2 incubation, the tissue was immersed in 96% alcohol for 60 minutes 3 times. The tissue was then immersed in 99% alcohol for 60 minutes 3 times, then twice in isoparafine for 60 minutes, twice in parafine for 60 minutes and the sample was allowed to cool down. The block was cut with a microtome into 4 microns sections and standard H&E staining was then carried out.

2.4. CT image acquisition and analysis

CT images of perfused and fixed whole mouse hearts were obtained using an Argus PET/CT preclinical scanner (SEDECAL, Madrid, Spain), with cone-beam geometry based on a tungsten anode x-ray tube and a digital CMOS X-ray detector. Imaging parameters were: Current: 340 µA; voltage: 40 kV; number of exposures per angle: 8; angular sampling: 1 projection per degree. The images were acquired and processed using the manufacturer software (MMWKS VISTA_PET/CT). Reconstruction used the FDK algorithm contained in Mangoose (GPU) software version 1.5, (SEDECAL, Madrid, Spain). The resulting 3D images showed a spatial resolution of 120x120x120 µm3, and the heart volumes were calculated by thresholding the 3D heart image from the surrounding air using MMWKS software analysis tools. The same threshold parameter was used for hearts before and after clearing.

2.5. Image acquisition with single plane illumination microscopy

3D stacks were acquired with a custom-built SPIM microscope. The illumination objective used to focus the laser light sheet onto the focal plane was an infinity-corrected 5x long working distance objective (Mitutoyo Corporation, Sakado, Japan, NA: 0.14, WD: 34 mm, Depth of focus (DF): 14 µm). Two other infinity-corrected long-working-distance magnification objectives (also from Mitutoyo) were used for detection: a 2x objective (NA:

0.055, WD: 34mm and DF: 91 µm) and a 5x objective similar to that used for illumination. The laser light was guided by mirrors towards the cylindrical lens that forms the light sheet. The light sheet passed through the illumination objective which focuses it inside the glass cuvette in which the sample is located. The sample is moved plane by plane (z-direction) with the help of a high-precision step motor (Zaber, Canada). The emitted light passed through the detection objective and the emission filter and was captured by a Neo 5.5 sCMOS camera (Andor, Belfast, UK) with 2560´2160 active pixels and a physical detector size of 6.5 µm x 6.5 µm. Additional details on the system can be found in [12].

Image acquisition with SPIM was controlled by a custom-made controlling software. After placing the sample in the field of view (FOV), the software allows the user to program a sequence of excitation lasers and their respective emission filters, as well as stage movements. Furthermore, the user sets parameters such as power of excitation laser, camera exposure time, initial and final z-positions and spacing between consecutive acquisitions.

2.6. Image processing

FIJI software was used to analyze the images [13]. In-house developed software was used to remove stripe artefacts and to align the lasers. The 3Dslicer software was used to for 3D volume rendering [14].

For correcting the inhomogeneous illumination, we compared the “N4-algorithm” [15] implemented in 3DSlicer with a specific algorithm developed in-house, based on performing a multiplicative correction of the pixel values with an exponential factor that increases along the direction of the light sheet path, according to attenuation coefficients obtained from the Beer-Lambert law. This latter algorithm proved to achieve a better illumination correction, assessed by drawing intensity profiles on the processed images.The images acquired with the SPIM microscope present some intrinsic artefacts that must be sorted out to enhance image quality. The progressive degradation of signal strength due to the light scattering and absorption derives in a decrease of image illumination. This illumination artifact typical of SPIM image stacks was corrected by applying a multiplicative correction factor matrix calculated assuming exponential laser light intensity loss while traversing the tissue (Fig. 3(A)), according to the following equation [16]:

$$cf_{(\Delta x)} = \frac{1}{e^{(-\mu_x \Delta x)}}$$

Where μ_x stands for for the attenuation coefficient previously obtained from the Beer-Lambert-law.

For a better identification of the labeled vasculature, we also applied a background subtraction followed by a maximum entropy thresholding.

3. Results and discussion

This section presents the different effect of CUBIC- and BABB-clearing methods on physical properties of cardiac tissue such as transparency, volume and weight. The effect of these methods on the cellular and subcellular structure are compared using fluorescence microscope and electron microscope images of cleared and uncleared cardiac tissue. Finally, we present 3D images of the cardiac vasculature processed with the illumination correction algorithm.

3.1. CUBIC and BABB-clearing of adult mouse heart

CUBIC and BABB are the tissue clearing methods widely preferred over other methods [6, 17]. To determine the ideal clearing method for the adult heart, we used both protocols to clear adult myocardium and compared their impact on the physical, cellular and subcellular characteristics of the tissue. Heart volume and weight were measured before, during and after tissue clearing with CUBIC and BABB. The volume was measured using CT (Computed Tomography) images of the hearts and the weight was determined with a scientific scales. Volume and weight of CUBIC-cleared hearts increased by 33% at the end of the protocol, while BABB-cleared hearts showed a 20% volume decrease in volume and weight (Fig. 1(E) and 1(F)).The decrease in volume and weight with BABB clearing may depend on the drastic dehydration due to the immersion in benzyl benzoate and benzyl alcohol

To determine the effects of both clearing protocols on the tissue cytoarchitecture, myocardial sections of three sample groups (uncleared, CUBIC-cleared and BABB-cleared) were analyzed by hematoxylin and eosin staining (H&E). A slight swelling of the cells was appreciated after CUBIC-clearing, compared to the uncleared tissue. This is likely to be caused by Reagent 1, which has been described to remove lipids, causing cell membrane interruption and allowing fluids to diffuse inside cells freely [10, 18]. (Fig. 2(A)). However, clearance with BABB led to changes in the tissue cytoarchitecture, including tissue disruption. To study changes at a subcellular level, we also carried out a Transmission Electron Microscopy (TEM) analysis. Although the general cell and scaffold structure was preserved in the CUBIC-cleared tissue, some differences in image contrast were evident (Fig. 2(B)), especially concerning mitochondria (see orange arrows) and nuclear membranes (green arrows). Additionally, new “spherical holes” appeared in the CUBIC cleared tissue (red arrows Fig. 2(B)). In TEM-microscopy the samples are stained with osmium tetroxide, which binds to lipids. Since most lipids were removed by the immersion in CUBIC’s R1, this is likely the cause of TEM image contrast decrease [19, 20]. On the other hand, the TEM-images of BABB-cleared cardiac tissue show tissue degeneration and empty spaces in between cell compartments, substantial tissue degeneration in form of spaces between cells (yellow arrows Fig. 2(B)) as well as sub-cellular alterations, also visible in the H&E-images. Images also showed a general contrast loss and accumulation of osmium tetroxide in the nuclei. These results are in agreement with the changes in volume and weight observed in Fig. 1. Taken together, they suggest that the CUBIC clearing protocol represents a less aggressive option to clear adult myocardial tissue, as it preserves the cardiac tissue integrity at a cellular and subcellular level much better than the BABB clearing method.

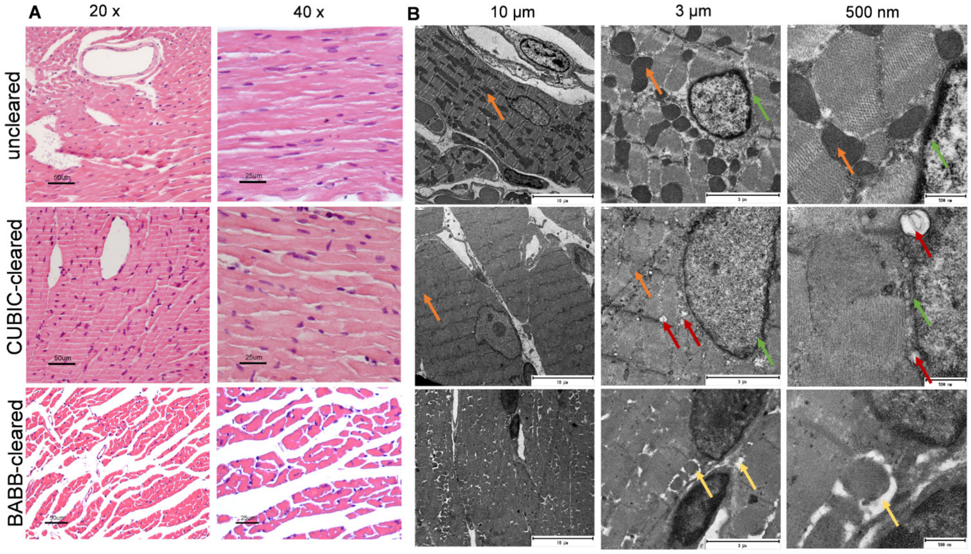

Fig. 2. CUBIC- and BABB-clearing in cardiac tissue at cellular- and subcellular level. A, Hematoxylin and eosin staining (H&E) of uncleared heart tissue in 20x and 40x magnification (upper row), CUBIC-cleared tissue (middle) and BABB-cleared tissue (bottom). B, Electron microscopy images of uncleared, CUBIC- and BABB-cleared cardiac tissue. Scale bars, 10 µm (left), 3 µm (middle) and 500 nm (right). Green and orange arrows indicate contrast loss; red arrows indicate, formation of cavities.

3.2. Illumination correction in SPIM-images

The program implemented in MATLAB for the illumination artefact correction was validated by comparing its results with those provided by the "N4"-algorithm implemented in 3DSlicer [21]. For validating the illumination correction, intensity profiles were plotted along the yellow lines shown in Fig. 3(A). The plot in Fig. 3(B) shows the intensity profiles of the original image (blue), the illumination-corrected image with our algorithm (green) and the intensity value profile of the image corrected with the N4-algorithm (red). Comparing intensity profiles of the three images we observe an improvement of an increase of 2 times in the intensity values of the N4-algorithm corrected image (red) (Fig. 3(B)) and an improvement of 3 times in the illumination-corrected image with our algorithm (green).(Fig. 3(B)). Therefore, the best result is achieved with our illumination correction algorithm (green) which makes use of the attenuation coefficient measured directly in the sample (Fig. 3(B)).

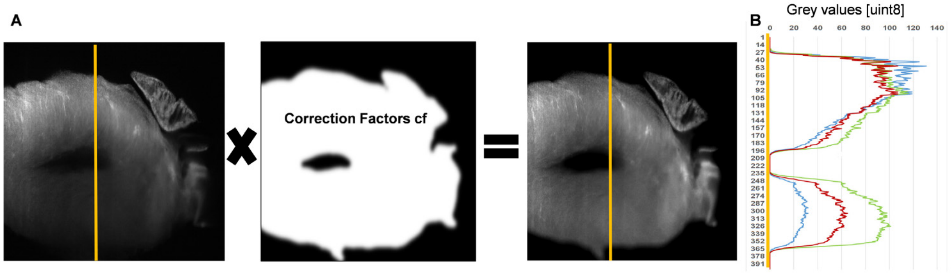

Fig. 3. Illumination correction of SPIM images. A, Schematic representing the multiplication of the original image. The intensity loss in y (left) with the correction factor matrix (middle) leads to the illumination-corrected image (right). B, Intensity profiles along the yellow lines shown in the images in A. Blue, Intensity profile along the yellow line of the original SPIM image where the intensity loss along the light path can be observed. Red, Intensity profile of the N4-algorithm corrected image. Green, Intensity profile of the image that was corrected using the described algorithm implemented in Matlab. All images show the 405 nm laser excitation channel (DAPI), in which the highest Rayleigh scattering is present.

3.3. Heart vasculature labelling and imaging

Compared to other mouse organs, the myocardium is a rather solid muscular tissue with a very tough texture that makes it difficult to clear and precludes efficient antibody penetration. On the other hand, the clearing protocol must be compatible with the labeling method of choice. Here we intend to visualize vascular architecture by combining a clearing method with blood vessel labeling of the whole mouse heart. The CUBIC protocol had previously demonstrated to render the best transparency compared to other clearing methods for the embryonic mouse heart. Here, we optimized the protocol for adult heart by reducing the immersion periods in the clearing reagents to minimize tissue processing times, while still achieving the desirable transparency (Fig. 1(A)). Although the highest transparency was achieved after the immersion in R1 rather than R2 (Fig. 1(C)), for SPIM-imaging the R2 treatment is necessary because after R1 the tissue is still dense and heterogeneous and leads to artifacts in SPIM images that need very tedious and time-consuming post-processing. The sample immersion in R2 matches the refractive index of the tissue with that of the immersion oil of the cuvette.

To study the distribution of the macro- and microvasculature, we compared two different approaches, immunohistochemistry with an anti-CD31 antibody and i.v. injection of fluorescently-labeled-lectins. Antibody penetration into the tissue was assessed through measurements on SPIM images. We found that the antibody penetrated up to 550 µm into the myocardium from both sides of the cardiac wall. Even though the antibody did not penetrate the entire cardiac tissue, a 3D reconstruction of the heart vessels could be achieved with the protocol proposed here [Visualization 1, Figs. 4(A), 4(B)).

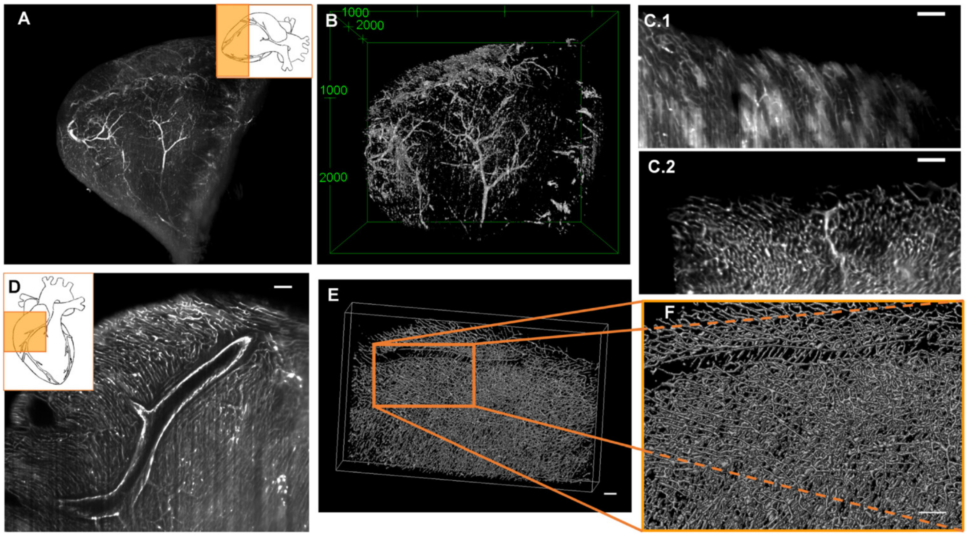

Fig. 4. 3D imaging of the vasculature obtained with SPIM. A, Maximum intensity projection of an anti-CD31 labeled mouse heart apex. SPIM-excitation laser, 635nm; emission filter, 670 nm. B, 3D-visualization the same data shown in A. C.1, Single SPIM image of a FITC-lectin labeled mouse heart. The low contrast between background (BG) and labeled vasculature makes it difficult to distinguish between them. Autofluorecence and stripes artifact harm the image quality. C.2, SPIM-image of a lectin-647 labeled mouse heart. The BG is minimized significantly by the absence of autofluorecence in the far-red channel. The stripes artifact almost entirely disappear. D, Single image of a SPIM image stack in which the macro- and micro-vasculature were both labeled with FITC-lectin (white). E, 3D volume rendering of the stained vasculature, stack size: 1945x1214x380 mm, visualized with VolView3 software (Bangham laboratory). F, Zoom of the indicated zone in E. All scale bars in all images, 100µm.

The limitations of antibody penetration due to the nature of the myocardial tissue were overcome by using other method to label blood vessels, the injection of fluorescently-labeled lectins (Figs. 4(C), 4(F)). The perfusion with these lectins improved the vasculature labelling compared to the antibody, especially for the microvasculature [Visualization 2, FITC-lectin labeled cardiac tissue] and [Visualization 3, lectin-647 labeled cardiac tissue]. Thus, due to lower attenuation and higher penetration depth of the laser at the excitation wavelength of 635 nm, far-red fluorophores like 649 reduce autofluorescence of the cardiac tissue albeit slightly reducing the overall resolution [9]. As shown in Figs. 4(E) and 4(F), the use of 649-lectin significantly improved image quality compared to FITC-lectin, achieving more continuous labelling of microvessels, less background and a wide field of view.

The images demonstrate the high resolution that can be achieved with just a 5x objective, and the quality with which the microvasculature of the cardiac tissue can be visualized. Nevertheless a study of subtle differences at higher magnification would be desirable.

4. Conclusions

To our knowledge, we present for the first time a reliable protocol to visualize in 3D the whole heart adult mouse vasculature. The combination of vasculature labelling, clearing protocols and 3D image acquisition with SPIM provide complete and valuable information on the spatial distribution of the vasculature that may cast light on the vascular remodeling that takes place in coronary artery diseases. We show that the CUBIC clearing protocol preserves cell integrity better than BABB that severely compromises tissue integrity.

SPIM image acquisition offers the possibility to image relatively large specimens (size up to various mm) in µm resolution, with short acquisition times and reduced photobleaching [22].In our study, SPIM was used to achieve an improved 3D visualization that may contribute to a more complete understanding of the vasculature architecture of the adult mouse heart.

This imaging protocol for the adult cardiac vasculature paves the way for a more accurate study of the vascular remodeling that takes place in the damaged heart. It will also allow the investigation of the impact of different drugs and treatments on the vasculature. Furthermore, the pipeline proposed here can be adapted to study the vascular tree of other organs and the changes they undergo following different types of injury.

Translational and biomedical applications may arise from this novel technology in the fields of cardiovascular and aging research.

Funding

Human Frontiers Scientific Program (RGP0004/2013); Red Cardiovascular (RIC) (RD12/0042/0057) ISCIII, Ministerio de Economía y Competitividad; Centro de Investigación Biomédica en Red de Salud Mental; EC FP7 CIG grant HIGH THROUGHPUT TOMO; BRADE, S2013/ICE-2958 (Comunidad de Madrid); Fondos FEDER "Una manera de hacer Europa"; MINECO grant FIS2016-77892-R; Pro-CNIC Foundation; Severo Ochoa Center of Excellence (MINECO award SEV-2015-0505).

Acknowledgments

We are grateful to Alexandra de Francisco, Yolanda Sierra, Ana Romero and Fernando Asensio for assisting with the perfusion experiments, Paloma Sánchez-Mateos for helping with microscopy images; Fernando Escolar (Centro de Investigaciones Biológicas, Madrid) for TEM images and Jose Manuel Lara in Servicio de Anatomia Patológica of HGUGM, Madrid for H&E stainings.

Disclosures

The authors declare that there are no conflicts of interest related to this article.

All experimental procedures were conducted in conformity with European Union Directive 2010/63/EU and were approved by the Ethics Committee for Animal Experimentation of hospital (Comité de Ética en Experimentación Animal, CEEA; number ES280790000087).